IEICE TRANS. ELECTRON., VOL.E107–C, NO.8 AUGUST 2024

PAPER

Method for Estimating Scatterer Information from the Response Waveform of a Backward Transient Scattering Field Using TD-SPT

Keiji GOTO[†a)], **Toru KAWANO**[†], ***Members***, **Munetoshi IWAKIRI**[†], **Tsubasa KAWAKAMI**[†], ***and*** **Kazuki NAKAZAWA**[†], ***Nonmembers***

SUMMARY This paper proposes a scatterer information estimation method using numerical data for the response waveform of a backward transient scattering field for both E- and H-polarizations when a two-dimensional (2-D) coated metal cylinder is selected as a scatterer. It is assumed that a line source and an observation point are placed at different locations. The four types of scatterer information covered in this paper are the relative permittivity of a surrounding medium, the relative permittivity of a coating medium layer and its thickness, and the radius of a coated metal cylinder. Specifically, a time-domain saddle-point technique (TD-SPT) is used to derive scatterer information estimation formulae from the amplitude intensity ratios (AIRs) of adjacent backward transient scattering field components. The estimates are obtained by substituting the numerical data of the response waveforms of the backward transient scattering field components into the estimation formulae and performing iterative calculations. Furthermore, a minimum thickness of a coating medium layer for which the estimation method is valid is derived, and two kinds of applicable conditions for the estimation method are proposed. The effectiveness of the scatterer information estimation method is verified by comparing the estimates with the set values. The noise tolerance and convergence characteristics of the estimation method and the method of controlling the estimation accuracy are also discussed.

key words: *scatterer information estimation method, response waveform, backward transient scattering field, time-domain saddle-point technique (TD-SPT), amplitude intensity ratios (AIRs)*

1. Introduction

Since the publication of Keller's paper until today, a number of researchers have presented various research results on the problem of electromagnetic scattering by two-dimensional (2-D) cylindrical objects [1]–[19]. The 2-D cylindrical objects are classified as metallic cylinders [1]–[4], [6], [8], [9], [14], dielectric cylinders [10], [13], [15], and coated metal cylinders [5], [7], [10]–[12], [16]–[19]. Typical examples of applications include the estimation of radar cross sections (RCSs) of objects such as aircraft [2]–[11], [14], [15] and the non-destructive deterioration diagnosis of reinforced concrete [17]–[19].

When an object is illuminated with a pulse wave, transient scattering waves are reemitted from the object. A response waveform of a transient scattering field contains scatterer information such as the structure, dimensions, and material of a scatterer. Research results on transient scattering fields from 2-D coated metal cylinders [12], [17]–[19] have made it possible to calculate response waveforms with high accuracy. However, these research results are difficult to analytically extract the transient scattering field components with different propagation paths that constitute the response waveforms.

The authors have derived high-frequency (HF) asymptotic solutions for a transient scattering field from a coated metal cylinder, namely a time-domain asymptotic-numerical solution (TD-ANS) [20]–[22], a TD saddle-point technique (TD-SPT) [23], [24], and a TD Fourier transform method (TD-FTM) [25], [26]. The HF asymptotic solutions for a backward transient scattering field [22]–[26] are represented by a superposition of a direct geometric optical ray (DGO) and a reflected GO (RGO) series. As a *first step* to estimate the scatterer information, we considered an interpretation method for the inversion phenomena of the response waveforms [23]. As a *second step*, we investigated an interpretation method for the amplitude intensities of the response waveforms [26].

The purpose of this paper is to propose a scatterer information estimation method using numerical data for the response waveform of a backward transient scattering field for both E- and H-polarizations when a 2-D coated metal cylinder is selected as a scatterer [27]. A line source and an observation point are assumed to be placed at different locations. The four types of scatterer information covered in this paper are the relative permittivity of a surrounding medium, the relative permittivity of a coating medium layer and its thickness, and the radius of a coated metal cylinder.

Specifically, scatterer information estimation formulae are to be derived from the amplitude intensity ratios (AIRs) of adjacent backward transient scattering field components using the TD-SPT [23]. The numerical data of the response waveforms of the backward transient scattering field components will be substituted into the estimation formulae and iterative calculations will be performed to obtain estimates. In addition, we will derive a minimum thickness of a coating medium layer for which the estimation method is valid, and propose two kinds of applicable conditions for the estimation method. The effectiveness of the scatterer information estimation method will be verified by comparing the estimates with the set values. The noise tolerance and convergence characteristics of the estimation method and the method of controlling the estimation accuracy will be also discussed.

The time dependence $\exp(-i\omega t)$ is assumed but sup-

Manuscript received September 3, 2023.
Manuscript revised December 12, 2023.
Manuscript publicized January 23, 2024.

[†]The National Defense Academy of Japan, Yokosuka-shi, 239–8686 Japan.
a) E-mail: keigoto@nda.ac.jp

DOI: 10.1587/transele.2023ECP5040

pressed throughout the text.

2. Formulation

Figure 1 shows a cross-sectional geometry of a 2-D coated metal cylinder of radius $\rho = a\ (= b + h)$, which is made of a metal cylinder of radius $\rho = b$ coated with a coating medium 2 (ε_2, μ_0) of thickness $h\ (= a - b)$, and coordinate systems (x, y, z) and (ρ, ϕ). The symbol ε_2 is a permittivity defined by $\varepsilon_2 = \varepsilon_0\varepsilon_{2r}$ where ε_{2r} is a relative permittivity. The constitutive parameters ε_0 and μ_0 are a permittivity and a permeability in free space, respectively. An electric or magnetic line source $\mathrm{Q}(\rho_0, \phi_0)$ is placed parallel to the central axis of the coated metal cylinder in a surrounding medium 1 (ε_1, μ_0), where ε_1 is defined by $\varepsilon_1 = \varepsilon_0\varepsilon_{1r}$ and ε_{1r} is a relative permittivity. An observation point $\mathrm{P}(\rho \neq \rho_0,\ \phi = \phi_0)$ in the medium 1 is placed at a different location from the line source Q. The permittivity of medium 1 and that of medium 2 are both assumed to be lossless and $\varepsilon_1 < \varepsilon_2$. The thickness h of the coating medium 2 is assumed to be greater than or equal to a minimum thickness h_c, namely $h \geq h_c$ (see (26) and (27)), which satisfies the applicable condition of the estimation method (see Sect. 4.4).

Figure 2 shows the propagation paths of the DGO and RGO components (⟶: solid curve with arrow) when a cylindrical pulse wave emitted from the line source Q is incident perpendicularly on a coated metal cylinder.

3. AIRs Using the TD-SPT

3.1 UWB Pulse Source

We assume a truncated Gaussian-type modulated pulse source $s(t)$ placed at the point Q [20]–[23], [27]

$$s(t) = \begin{cases} \exp\left[-i\omega_0(t - t_0) - \dfrac{(t - t_0)^2}{(2d)^2}\right] & \text{for } 0 \leq t \leq 2t_0 \\ 0 & \text{elsewhere} \end{cases} \tag{1}$$

where ω_0 is a central angular frequency, and t_0 and d are constant parameters. The frequency spectrum $S(\omega)$ of $s(t)$ is given by the following equation using the error function erf z [28].

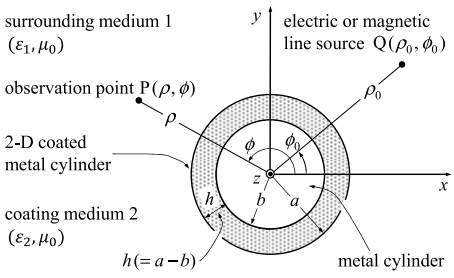

Fig. 1 2-D coated metal cylinder, and coordinate systems (x, y, z) and (ρ, ϕ). $\mathrm{Q}(\rho_0, \phi_0)$: electric or magnetic line source, $\mathrm{P}(\rho, \phi)$: observation point.

$$S(\omega) = 2d\sqrt{\pi}\,\mathrm{Re}[\mathrm{erf}\,\beta(\omega)]\exp\{i\omega t_0 - d^2(\omega - \omega_0)^2\} \tag{2}$$

$$\beta(\omega) = \frac{t_0}{2d} - id(\omega - \omega_0) \tag{3}$$

$$\mathrm{erf}\,z = \frac{2}{\sqrt{\pi}}\int_0^z \exp(-t^2)dt. \tag{4}$$

Figures 3 (a) and 3 (b) show the real part of $s(t)$ and the absolute value of $S(\omega)$, respectively. The numerical parameters used in the calculations are given in the caption of Fig. 3. For these numerical parameters, the fractional bandwidth (FB) of $S(\omega)$ is 0.34, which satisfies the ultra-wideband (UWB) definition (FB > 0.25) [29]. Therefore, $s(t)$ in Fig. 3 is a UWB pulse source.

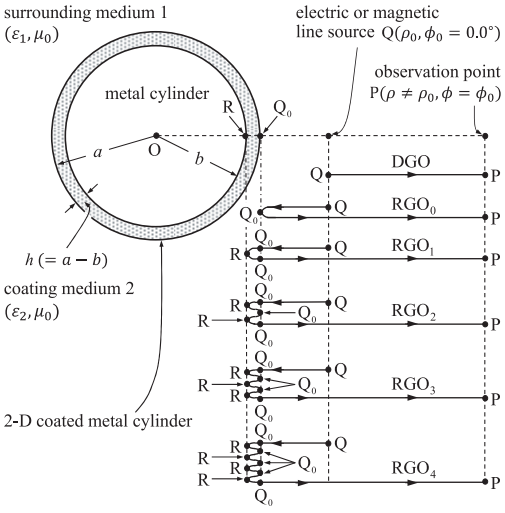

Fig. 2 Schematic diagram of backward transient scattering from a 2-D coated metal cylinder. Location of the electric or magnetic line source $\mathrm{Q}(\rho_0,\ \phi_0 = 0.0°)$ and that of the observation point $\mathrm{P}(\rho \neq \rho_0,\ \phi = \phi_0)$. The propagation paths of backward transient scattering field components: $\mathrm{DGO(Q{\to}P)}$, $\mathrm{RGO}_{p=0} = \mathrm{RGO_0(Q{\to}Q_0{\to}P)}$, $\mathrm{RGO}_{p=1} = \mathrm{RGO_1(Q{\to}Q_0{\to}R{\to}Q_0{\to}P)}$, and $\mathrm{RGO}_p\mathrm{(Q{\to}}p\mathrm{(Q_0{\to}R{\to})Q_0{\to}P)}$. The propagation path $p(\mathrm{Q_0{\to}R{\to}})\mathrm{Q_0}$ indicates multiple reflection effect in a coating medium 2. The p denotes the number of reflections at the point R on a metal surface of radius $\rho = b$.

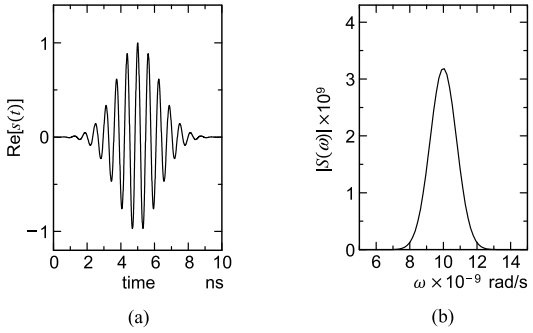

Fig. 3 Truncated Gaussian-type modulated UWB pulse source $s(t)$ defined by (1). (a) Real part of $s(t)$. (b) Absolute value of $S(\omega)$. Numerical parameters: $\omega_0 = 1.0 \times 10^{10}$ rad/s, $t_0 = 5.0 \times 10^{-9}$ s, $d = 9.0 \times 10^{-10}$ s, and FB = 0.34.

3.2 Derivation of the AIRs Using the TD-SPT

The backward transient scattering field component in (A· 2) shown in Appendix, which constitutes the TD-SPT in (A· 1), takes a peak and its arrival time of the response waveform $\mathrm{Re}[y_{j,\mathrm{SPT},\ell}(t)]$, $j = \mathrm{E},\mathrm{H}$ as follows [27]

$$\mathrm{Re}[y_{j,\mathrm{SPT},\ell}(t_\ell)] = \mathrm{Re}[D(\omega_0)]A_{j,\ell}\,\mathrm{erf}\,\beta(\omega_0), \quad \ell = \mathrm{DGO}, \mathrm{RGO}_p,\ p = 0, 1, \cdots, M_j \tag{5}$$

$$t = t_\ell = t_0 + \frac{L_\ell}{c_1}. \tag{6}$$

In obtaining (5) from (A· 2), we used the following relation

$$\omega_{s,\ell} = \omega_0 \quad \text{for } t = t_\ell. \tag{7}$$

In the following, the AIRs for adjacent backward transient scattering field components are derived using the TD-SPT [27].

First, we derive the $\mathrm{AIR}_{j,\mathrm{RGO}_0/\mathrm{DGO}}$, $j = \mathrm{E},\mathrm{H}$ of the $\mathrm{RGO}_{p=0}$ (= RGO_0) to the DGO. Applying (A· 6) and (A· 9) to (5), the $\mathrm{AIR}_{j,\mathrm{RGO}_0/\mathrm{DGO}}$ is given by

$$\begin{aligned}\mathrm{AIR}_{j,\mathrm{RGO}_0/\mathrm{DGO}} &= \frac{\mathrm{Re}[y_{j,\mathrm{SPT},\mathrm{RGO}_0}(t_{\mathrm{RGO}_0})]}{\mathrm{Re}[y_{j,\mathrm{SPT},\mathrm{DGO}}(t_{\mathrm{DGO}})]} \\ &= \frac{\mathrm{Re}[D(\omega_0)]A_{j,\mathrm{RGO}_0}\,\mathrm{erf}\,\beta(\omega_0)}{\mathrm{Re}[D(\omega_0)]A_{j,\mathrm{DGO}}\,\mathrm{erf}\,\beta(\omega_0)} \\ &= \sqrt{\frac{a(L_> - L_<)}{aL_< + aL_> + 2L_< L_>}}R_{j,11}\end{aligned} \tag{8}$$

where $L_<$ ($L_>$) is a symbol for the smaller (larger) in L_1 (= QQ_0) and L_2 (= $\mathrm{Q}_0\mathrm{P}$) in (A· 12) (see Fig. 2). The square root term is a divergence factor. The $\mathrm{AIR}_{j,\mathrm{RGO}_0/\mathrm{DGO}}$ is represented by the product of two influence factors, namely the divergence factor and the reflection factor $R_{j,11}$ (see (A· 13)).

Second, we derive the $\mathrm{AIR}_{j,\mathrm{RGO}_1/\mathrm{RGO}_0}$, $j = \mathrm{E},\mathrm{H}$ of the $\mathrm{RGO}_{p=1}$ (= RGO_1) to the $\mathrm{RGO}_{p=0}$(= RGO_0). Applying (A· 9) and (A· 14) to (5), the $\mathrm{AIR}_{j,\mathrm{RGO}_1/\mathrm{RGO}_0}$ is represented by

$$\begin{aligned}\mathrm{AIR}_{j,\mathrm{RGO}_1/\mathrm{RGO}_0} &= \frac{\mathrm{Re}[y_{j,\mathrm{SPT},\mathrm{RGO}_1}(t_{\mathrm{RGO}_1})]}{\mathrm{Re}[y_{j,\mathrm{SPT},\mathrm{RGO}_0}(t_{\mathrm{RGO}_0})]} \\ &= \frac{\mathrm{Re}[D(\omega_0)]A_{j,\mathrm{RGO}_1}\,\mathrm{erf}\,\beta(\omega_0)}{\mathrm{Re}[D(\omega_0)]A_{j,\mathrm{RGO}_0}\,\mathrm{erf}\,\beta(\omega_0)} \\ &= \sqrt{\frac{aL_< + aL_> + 2L_< L_>}{aL_< + aL_> + 2L_< L_> + D_1}} \\ &\quad \cdot (T_{j,12}T_{j,21})\left(\frac{R_{j,2}}{R_{j,11}}\right).\end{aligned} \tag{9}$$

The $\mathrm{AIR}_{j,\mathrm{RGO}_1/\mathrm{RGO}_0}$ is expressed as the product of three influence factors, namely the divergence factor, the transmission factor ($T_{j,12}T_{j,21}$) (see (A· 18) and (A· 19)), and the reflection factor ($R_{j,2}/R_{j,11}$) (see (A· 13) and (A· 20)).

Finally, we derive the $\mathrm{AIR}_{j,\mathrm{RGO}_p/\mathrm{RGO}_{p-1}}$, $j = \mathrm{E},\mathrm{H}$, $p = 2, 3, \cdots, M_j$ of the RGO_p to the RGO_{p-1}. Applying (A· 14) to (5), the $\mathrm{AIR}_{j,\mathrm{RGO}_p/\mathrm{RGO}_{p-1}}$ is given by

$$\begin{aligned}\mathrm{AIR}_{j,\mathrm{RGO}_p/\mathrm{RGO}_{p-1}} &= \frac{\mathrm{Re}[y_{j,\mathrm{SPT},\mathrm{RGO}_p}(t_{\mathrm{RGO}_p})]}{\mathrm{Re}[y_{j,\mathrm{SPT},\mathrm{RGO}_{p-1}}(t_{\mathrm{RGO}_{p-1}})]} \\ &= \frac{\mathrm{Re}[D(\omega_0)]A_{j,\mathrm{RGO}_p}\,\mathrm{erf}\,\beta(\omega_0)}{\mathrm{Re}[D(\omega_0)]A_{j,\mathrm{RGO}_{p-1}}\,\mathrm{erf}\,\beta(\omega_0)} \\ &= \sqrt{\frac{aL_< + aL_> + 2L_< L_> + D_{p-1}}{aL_< + aL_> + 2L_< L_> + D_p}} \\ &\quad \cdot (R_{j,2}R_{j,22}), \quad p = 2, 3, \cdots, M_j.\end{aligned} \tag{10}$$

The $\mathrm{AIR}_{j,\mathrm{RGO}_p/\mathrm{RGO}_{p-1}}$ is expressed as the product of two influence factors, namely the divergence factor and the reflection factor ($R_{j,2}R_{j,22}$) (see (A· 20) and (A· 21)).

4. Scatterer Information Estimation

4.1 Simulation Model

In this section, we propose a simulation model to be used in the scatterer information estimation method in Sect. 4.3. There are four types of scatterer information, namely the relative permittivity of the surrounding medium 1, the relative permittivity of the coating medium 2 and its thickness, and the radius of a coated metal cylinder.

4.1.1 Assumptions and Notations for Estimation

First, we assume the following (A) to (F) in the scatterer information estimation method.

(A) The structure of a scatterer is a 2-D coated metal cylinder coated with a uniform dielectric medium layer.
(B) A pulse source $s(t)$ in (1) and its numerical parameters (ω_0, t_0, d) are known.
(C) The pulse wave is radiated from a line source Q placed parallel to the central axis of a coated metal cylinder.
(D) The radius of a scatterer is sufficiently large compared to a wavelength of a central angular frequency ω_0 of a pulse source $s(t)$.
(E) A line source Q and an observation point P are placed at different locations and a distance L_{DGO} (= QP) between the point Q and the point P is known.
(F) At the observation point P, the peaks of the response waveforms of the backward transient scattering field components and their arrival times can be observed with high accuracy.

Second, the estimation method uses the following notations (Ȧ) and (Ḃ).

(Ȧ) Estimates are marked with a caret symbol (ˆ) and are denoted as $\hat{\varepsilon}_{1r}$, $\hat{\varepsilon}_{2r}$, $\hat{h}$, and $\hat{a}$.
(Ḃ) Numerical parameters and numerical data observed in the response waveforms are marked with an overline

symbol ($\overline{\ }$) and are denoted as $\overline{L}_{\mathrm{DGO}}$, $\bar{t}_0$, $\bar{t}_\ell$, and $\overline{\mathrm{Re}[y_{j,\mathrm{SPT},\ell}(\bar{t}_\ell)]}$.

4.1.2 Simulation Model and Numerical Data of Response Waveforms

Figure 4 (a) shows, as a simulation model for estimating the scatterer information, a diagram of a 2-D coated metal cylinder of radius $\hat{a}$ coated with a coating medium 2 $(\varepsilon_0\hat{\varepsilon}_{2r}, \mu_0)$ of thickness $\hat{h}$. A line source Q and an observation point P are placed at different locations in a surrounding medium 1 $(\varepsilon_0\hat{\varepsilon}_{1r}, \mu_0)$. The distance QP between the two points is $\overline{L}_{\mathrm{DGO}}$.

Figure 4 (b) shows an example of numerical data for three sets of response waveforms of the backward transient scattering electric field components calculated from the TD-SPT in (A· 1). The peak and arrival time of the DGO are $\overline{\mathrm{Re}[y_{\mathrm{E,SPT,DGO}}(\bar{t}_{\mathrm{DGO}})]}$ and $\bar{t}_{\mathrm{DGO}}$, respectively. While the peaks and their arrival times of the RGO_p, $p = 0, 1$ are $\overline{\mathrm{Re}[y_{\mathrm{E,SPT,RGO}_p}(\bar{t}_{\mathrm{RGO}_p})]}$ and $\bar{t}_{\mathrm{RGO}_p}$, respectively.

4.2 Derivation of Scatterer Information Estimation Formulae

In this section, we derive estimation formulae for four types of scatterer information $(\hat{\varepsilon}_{1r}, \hat{\varepsilon}_{2r}, \hat{h}, \hat{a})$.

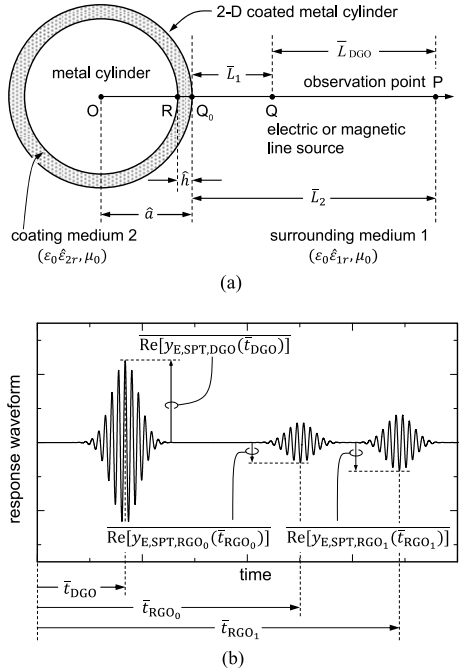

Fig. 4 Simulation model of a scatterer information estimation method. (a) Diagram of a 2-D coated metal cylinder, an electric or magnetic line source Q, an observation point P, a point Q_0 on a coating surface of radius $\hat{a}$, and a point R on a metal surface of radius $\hat{a} - \hat{h}$. (b) An example of numerical data for three sets of peaks of the response waveforms of the backward transient scattering electric field components and their arrival times calculated from the TD-SPT in (A· 1).

4.2.1 Estimation Formula $\hat{\varepsilon}_{1r}$ for Relative Permittivity ε_{1r}

Substituting (A· 4) into (6) gives

$$\hat{\varepsilon}_{1r} = \left[\frac{c_0}{\overline{L}_{\mathrm{DGO}}}(\bar{t}_{\mathrm{DGO}} - \bar{t}_0)\right]^2 \tag{11}$$

where c_0 is the speed of light in free space (see (A· 4)). In the derivation of $\hat{\varepsilon}_{1r}$ in (11), L_{DGO} (= QP) and t_{DGO}, and t_0 are replaced by the numerical data $\overline{L}_{\mathrm{DGO}}$ and $\bar{t}_{\mathrm{DGO}}$, and the numerical parameter $\bar{t}_0$, respectively.

4.2.2 Estimation Formula $\hat{\varepsilon}_{2r}$ for Relative Permittivity ε_{2r}

Substituting (A· 8), (A· 11), and (A· 12) into (6), we obtain

$$\overline{L}_1 = \frac{c_1}{2}(\bar{t}_{\mathrm{RGO}_0} - \bar{t}_{\mathrm{DGO}}) = \mathrm{QQ}_0 \tag{12}$$

$$\overline{L}_2 = \frac{c_1}{2}(\bar{t}_{\mathrm{RGO}_0} + \bar{t}_{\mathrm{DGO}} - 2\bar{t}_0) = \mathrm{Q}_0\mathrm{P} \tag{13}$$

where $\overline{L}_1$ ($\overline{L}_2$) is the distance QQ_0 ($\mathrm{Q}_0\mathrm{P}$) from the source point Q (point Q_0) to the point Q_0 (observation point P) (see Fig. 4 (a)).

Then, after substituting (A· 13) and (A· 18) to (A· 20) into (9), we obtain the following formula

$$\hat{\varepsilon}_{2r} = \left[\left(2\overline{\Lambda}_{1/0} + \sqrt{4\left(\overline{\Lambda}_{1/0}\right)^2 + \left(\overline{A}_{j,1/0}\right)^2}\right)\Big/\overline{A}_{j,1/0}\right]^2 \hat{\varepsilon}_{1r} \tag{14}$$

$$\overline{\Lambda}_{1/0} = \sqrt{\frac{\hat{a}\overline{L}_< + \hat{a}\overline{L}_> + 2\overline{L}_<\overline{L}_>}{\hat{a}\overline{L}_< + \hat{a}\overline{L}_> + 2\overline{L}_<\overline{L}_> + \overline{D}_1}} \tag{15}$$

$$\overline{D}_{p=1} = \overline{D}_1 = \frac{(\hat{a} + \overline{L}_<)(\hat{a} + \overline{L}_>)(2\hat{h})}{\hat{a} - \hat{h}}\sqrt{\frac{\hat{\varepsilon}_{1r}}{\hat{\varepsilon}_{2r}}} \tag{16}$$

$$\overline{A}_{j,1/0} = \overline{\mathrm{AIR}_{j,\mathrm{RGO}_1/\mathrm{RGO}_0}} = \frac{\overline{\mathrm{Re}[y_{j,\mathrm{SPT,RGO}_1}(\bar{t}_{\mathrm{RGO}_1})]}}{\overline{\mathrm{Re}[y_{j,\mathrm{SPT,RGO}_0}(\bar{t}_{\mathrm{RGO}_0})]}} \tag{17}$$

where $\overline{L}_<$ ($\overline{L}_>$) is a symbol for the smaller (larger) in the numerical data $\overline{L}_1$ in (12) and $\overline{L}_2$ in (13). In the derivation of $\overline{D}_1$ in (16), a, ε_{1r}, h and ε_{2r}, and $L_<$ and $L_>$ are replaced by estimates $\hat{a}$, $\hat{\varepsilon}_{1r}$, $\hat{h}$, and $\hat{\varepsilon}_{2r}$, and numerical data $\overline{L}_<$ and $\overline{L}_>$, respectively. The symbols $\overline{\Lambda}_{1/0}$ in (15) and $\overline{A}_{j,1/0}$ in (17) are numerical data of the divergence factor and $\mathrm{AIR}_{j,\mathrm{RGO}_1/\mathrm{RGO}_0}$, respectively. Therefore, by substituting $\hat{\varepsilon}_{1r}$, $\overline{A}_{j,1/0}$, and $\overline{\Lambda}_{1/0}$ into (14), we numerically obtain the estimate of $\hat{\varepsilon}_{2r}$.

While $\hat{\varepsilon}_{2r}$ in (14) can be simplified as follows by approximating $\overline{\Lambda}_{1/0}$ in (15) with one

$$\hat{\varepsilon}_{2r} \sim \left[\left(2 + \sqrt{4 + (\overline{A}_{j,1/0})^2}\right)\Big/\overline{A}_{j,1/0}\right]^2 \hat{\varepsilon}_{1r}. \tag{18}$$

4.2.3 Estimation Formula $\hat{h}$ for Thickness h

Substituting (A· 4) and (A· 17) into (6), we obtain

$$\hat{h} = \frac{c_0}{2\sqrt{\hat{\varepsilon}_{2r}}}(\bar{t}_{\mathrm{RGO}_1} - \bar{t}_{\mathrm{RGO}_0}). \tag{19}$$

In the derivation of $\hat{h}$ in (19), t_{RGO_0} and t_{RGO_1} are replaced by numerical data $\bar{t}_{\mathrm{RGO}_0}$ and $\bar{t}_{\mathrm{RGO}_1}$, respectively. Therefore, by substituting $\bar{t}_{\mathrm{RGO}_0}$, $\bar{t}_{\mathrm{RGO}_1}$, and $\hat{\varepsilon}_{2r}$ into (19), we numerically obtain the estimate of $\hat{h}$.

4.2.4 Estimation Formula $\hat{a}$ for Radius a

After substituting (A· 12), (A· 13), (12), and (13) into (8), we obtain the following formula

$$\hat{a} = \frac{2\overline{L}_< \overline{L}_>}{\overline{B}_{j,0/\mathrm{D}} - (\overline{L}_< + \overline{L}_>)} \tag{20}$$

$$\overline{B}_{j,0/\mathrm{D}} = \frac{\overline{L}_> - \overline{L}_<}{(\overline{A}_{j,0/\mathrm{D}})^2}\left(\frac{\sqrt{\hat{\varepsilon}_{2r}} - \sqrt{\hat{\varepsilon}_{1r}}}{\sqrt{\hat{\varepsilon}_{2r}} + \sqrt{\hat{\varepsilon}_{1r}}}\right)^2 \tag{21}$$

$$\overline{A}_{j,0/\mathrm{D}} = \overline{\mathrm{AIR}_{j,\mathrm{RGO}_0/\mathrm{DGO}}} = \frac{\overline{\mathrm{Re}[y_{j,\mathrm{SPT},\mathrm{RGO}_0}(\bar{t}_{\mathrm{RGO}_0})]}}{\overline{\mathrm{Re}[y_{j,\mathrm{SPT},\mathrm{DGO}}(\bar{t}_{\mathrm{DGO}})]}} \tag{22}$$

where $\overline{A}_{j,0/\mathrm{D}}$ is the numerical data of $\mathrm{AIR}_{j,\mathrm{RGO}_0/\mathrm{DGO}}$ obtained from Fig. 4 (b). In the derivation of $\hat{a}$ in (20), ε_{1r} and ε_{2r} are replaced by the estimates $\hat{\varepsilon}_{1r}$ and $\hat{\varepsilon}_{2r}$, respectively. Thus, by substituting $\overline{L}_<$, $\overline{L}_>$, $\overline{A}_{j,0/\mathrm{D}}$, $\hat{\varepsilon}_{1r}$, and $\hat{\varepsilon}_{2r}$ into (20), we numerically obtain the estimate of $\hat{a}$.

4.3 Scatterer Information Estimation Method

In this section, we propose a scatterer information estimation method using the estimation formulae which are derived in Sect. 4.2.

In (a) to (j) below, the methods for estimating four types of scatterer information are presented. The symbols ε and I_{MAX} denote on a convergence degree and an upper limit on the number of iterations, respectively.

(a) Substituting the numerical data $\overline{L}_{\mathrm{DGO}}$ and $\bar{t}_{\mathrm{DGO}}$, and the numerical parameter $\bar{t}_0$ into (11) gives an estimate of $\hat{\varepsilon}_{1r}$.

(b) Substituting the numerical data $\overline{A}_{j,1/0}$ in (17) and $\hat{\varepsilon}_{1r}$ in (a) into (18) gives an estimate of $\hat{\varepsilon}_{2r} = \hat{\varepsilon}_{2r,I}$. The subscript I is a symbol for the number of iterations.

(c) By substituting the numerical data $\bar{t}_{\mathrm{RGO}_0}$ and $\bar{t}_{\mathrm{RGO}_1}$, and the estimate $\hat{\varepsilon}_{2r,I}$ obtained in (b) into (19), we obtain an estimate of $\hat{h} = \hat{h}_I$.

(d) Substituting the numerical data $\overline{L}_<$, $\overline{L}_>$, and $\overline{A}_{j,0/\mathrm{D}}$ and the estimates $\hat{\varepsilon}_{1r}$ and $\hat{\varepsilon}_{2r,I}$ into (20) gives an estimate of $\hat{a} = \hat{a}_I$.

(e) We compute $\overline{D}_1$ in (16) using $\overline{L}_<$, $\overline{L}_>$, $\hat{\varepsilon}_{1r}$, $\hat{\varepsilon}_{2r}$, $\hat{h}$, and $\hat{a}$, and then update $\overline{\Lambda}_{1/0}$ in (15) using $\overline{L}_<$, $\overline{L}_>$, $\hat{a}$, and $\overline{D}_1$.

(f) By substituting the estimate $\hat{\varepsilon}_{1r}$ in (a) and the numerical data $\overline{\Lambda}_{1/0}$ and $\overline{A}_{j,1/0}$ into (14), we obtain an estimate $\hat{\varepsilon}_{2r} = \hat{\varepsilon}_{2r,I}$ with improved accuracy compared to that in (b).

(g) To count the number of iterations, we increase the value of I by one. We then obtain new estimates $\hat{h} = \hat{h}_{I+1}$, $\hat{a} = \hat{a}_{I+1}$, and $\hat{\varepsilon}_{2r} = \hat{\varepsilon}_{2r,I+1}$ in (c), (d), and (f). The calculations in (c), (d), (e), and (f) are iterated to improve the accuracy of estimates.

(h) We use the following equation to determine the convergence degree of the estimates.

$$\Delta\hat{X}_I = \left|\frac{\hat{X}_I - \hat{X}_{I-1}}{\hat{X}_I}\right| < \varepsilon \quad \text{for } X = \varepsilon_{2r}, h, a. \tag{23}$$

In (23), we consider convergence to the set value if the relative difference between the previous estimate $\hat{X}_{I-1}$ and the new estimate $\hat{X}_I$ is less than the convergence degree ε. After saving I in I_{END}, we proceed to (j).

(i) If I satisfies I_{MAX}, store I_{MAX} in I_{END} and then proceed to (j).

(j) Output estimates $(\hat{\varepsilon}_{1r}, \hat{\varepsilon}_{2r}, \hat{h}, \hat{a})$ and the number of iterations I_{END}.

4.4 Applicable Conditions of Estimation Method

In this section, we first propose a time-related applicable condition for the scatterer information estimation method. Next, we derive the minimum thickness h_c of a coating medium layer for which the scatterer information estimation method is valid, and propose a new application condition for the thickness of a coating medium layer.

The time t_2 required for a round trip through a coating medium layer of thickness h (see propagation path $\mathrm{Q}_0 \rightarrow \mathrm{R} \rightarrow \mathrm{Q}_0$ in Fig. 2) is given by the following formula using the speed of light c_2 in medium 2.

$$t_2 = \frac{2h}{c_2},\ c_2 = \frac{1}{\sqrt{\varepsilon_2\mu_0}} = \frac{c_0}{\sqrt{\varepsilon_{2r}}},\ c_0 = \frac{1}{\sqrt{\varepsilon_0\mu_0}}. \tag{24}$$

The condition that the peak $\mathrm{Re}[y_{j,\mathrm{SPT},\mathrm{RGO}_p}(t_{\mathrm{RGO}_p})]$ of the response waveform of the p-times reflected GO component in (5) does not combine with the adjacent $p+1$-times reflected GO component is the applicable condition of the estimation method. Therefore, the applicable condition is that the time t_2 in (24) is greater than or equal to one half of the pulse width ($2t_0$) of a pulse source $s(t)$ in (1) as follows

$$t_2 \geq t_0. \tag{25}$$

Substituting (24) into (25) gives the minimum thickness h_c as follows

$$h_c = \frac{t_0 c_2}{2} = \frac{t_0 c_0}{2\sqrt{\varepsilon_{2r}}}. \tag{26}$$

By using (26), the applicable condition of the estimation method to the thickness h of a coating medium layer is given by

$$h \geq h_c. \tag{27}$$

5. Numerical Results and Discussions

In this section, we first evaluate the accuracy and effectiveness of the TD-SPT and extract numerical data for three sets of backward transient scattering field components needed to estimate the scatterer information. Then, the effectiveness of the scatterer information estimation method is verified by comparing the estimates with the set values. The noise tolerance and convergence characteristics of the estimation method as well as the method of controlling the estimation accuracy are also discussed. In the following calculations, a common factor $D(\omega_0)$ in (A· 3), where ω is replaced by ω_0, is normalized by one ($D(\omega_0) = 1$).

5.1 Accuracy and Effectiveness of TD-SPT and Numerical Data Required for Estimation

Figures 5 (a) and 5 (b) show the response waveforms of the backward transient scattering fields for E- and H-polarizations, respectively. The numerical parameters used in the calculations are given in the caption of Fig. 5. In this case, the time t_2 required for a round trip through the coating medium layer is $t_2 > t_0$, and the thickness h of a coating medium layer is $h > h_c$. Therefore, the numerical parameters used in the calculations in Fig. 5 satisfy the two applicable conditions for the scatterer information estimation method. For visibility of the response waveforms, the vertical axes of the response waveforms shown on the left and right sides of Figs. 5 (a) and 5 (b) are shown by different

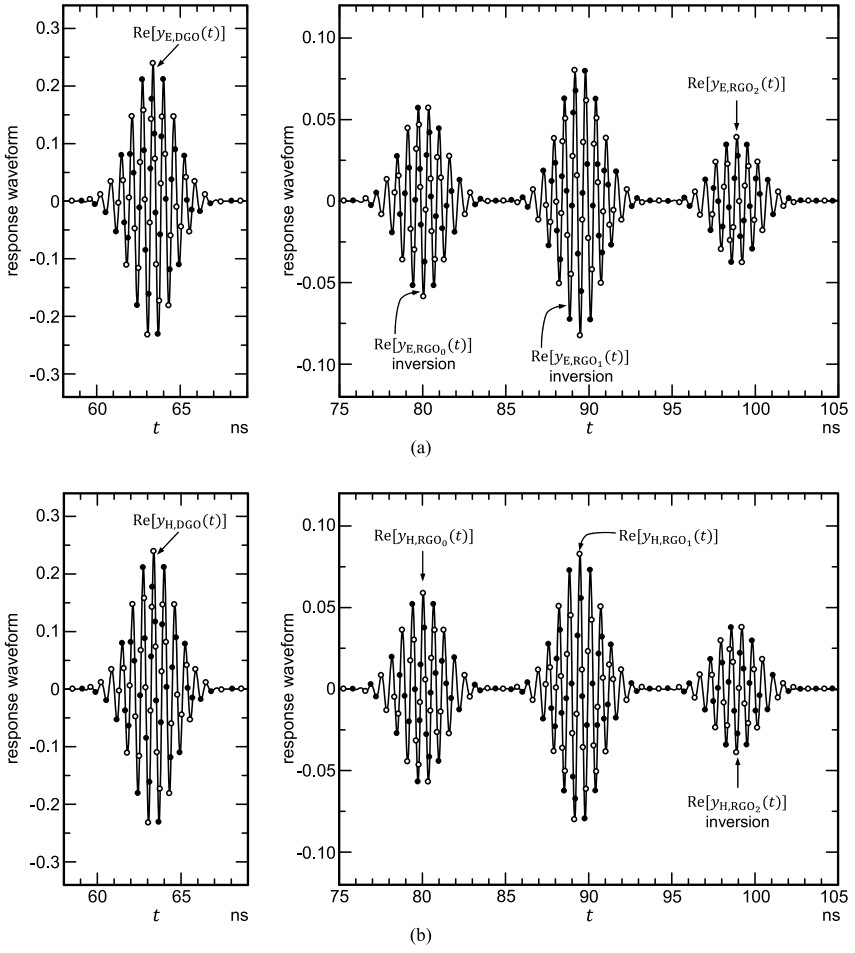

Fig. 5 Response waveforms of backward transient scattering fields for E- and H-polarizations under the condition $\varepsilon_1 < \varepsilon_2$. The numerical parameters used in the calculations are $a = 2.0$ m, $\varepsilon_1 = \varepsilon_0\varepsilon_{1r}$, $\varepsilon_{1r} = 1$, $\varepsilon_2 = \varepsilon_0\varepsilon_{2r}$, $\varepsilon_{2r} = 9$, $t_2 = 9.4248 \times 10^{-9}$ s $> t_0$ (= 5.0×10^{-9} s), and $h = 0.47091$ m (= $0.23546a$) $> h_c$ (= 0.24983 m (= $0.12491a$)). The source point Q(ρ_0, ϕ_0) = ($2.25a$, 0.0°), the observation point P(ρ, ϕ) = ($11.0a$, 0.0°), and the distance $\overline{L}_{DGO}$ (= QP) = $8.75a$. The pulse source $s(t)$ used in the calculations is the UWB pulse source shown in Fig. 3.
(a) ——: Re[$y_{E,TD\text{-}SPT}(t)$], ○ ○ ○: Re[$y_{E,reference}(t)$], ● ● ●: Re[$y_{E,TD\text{-}SPT}(t)$] when the locations of Q and P are swapped.
(b) ——: Re[$y_{H,TD\text{-}SPT}(t)$], ○ ○ ○: Re[$y_{H,reference}(t)$], ● ● ●: Re[$y_{H,TD\text{-}SPT}(t)$] when the locations of Q and P are swapped.

scales.

First, we evaluate the accuracy and effectiveness of the TD-SPT for E-polarization. In Fig. 5 (a), $\mathrm{Re}[y_{\mathrm{E,TD\text{-}SPT}}(t)]$ (——) set to $M_{\mathrm{E}} = 2$ (see (A· 1)) is in good agreement with the reference solution $\mathrm{Re}[y_{\mathrm{E,reference}}(t)]$ (∘ ∘ ∘) (see (6) in [26]) over the whole region. This allows us to verify the accuracy of the TD-SPT. The computation times of $\mathrm{Re}[y_{\mathrm{E,TD\text{-}SPT}}(t)]$ and $\mathrm{Re}[y_{\mathrm{E,reference}}(t)]$ are 0.0128 s and 0.2425 s, respectively. The computation speed ratio of the TD-SPT to the reference solution is 18.95, thereby confirming the effectiveness of the TD-SPT. In $\mathrm{Re}[y_{\mathrm{E,TD\text{-}SPT}}(t)]$ in (A· 1), the calculations when the locations of a source point Q and an observation point P are swapped are indicated by black circles (• • •). Since the black circles (• • •) are identical to the solid line (——), we can numerically confirm that the TD-SPT satisfies the reciprocity principle [30].

Next, the accuracy and effectiveness of the TD-SPT for H-polarization, shown in Fig. 5(b), can be discussed in the same way as those for E-polarization described above. In this way, we can confirm the accuracy and effectiveness of TD-SPT for H-polarization.

Table 1 shows the numerical data for the peaks of DGO and RGO_p, $p = 0, 1$ for both E- and H-polarizations and their arrival times. We observe that there are two relationships between the peaks for E-polarization and those for H-polarization, as follows

$$\overline{\mathrm{Re}[y_{\mathrm{E,SPT,DGO}}(\bar{t}_{\mathrm{DGO}})]} = \overline{\mathrm{Re}[y_{\mathrm{H,SPT,DGO}}(\bar{t}_{\mathrm{DGO}})]} \tag{28}$$

$$\overline{\mathrm{Re}[y_{\mathrm{E,SPT,RGO}_p}(\bar{t}_{\mathrm{RGO}_p})]} = -\overline{\mathrm{Re}[y_{\mathrm{H,SPT,RGO}_p}(\bar{t}_{\mathrm{RGO}_p})]}. \tag{29}$$

The sign inversions for the peaks of RGO_p, $p = 0, 1$ due to the polarization difference shown in (29) can be observed in Fig. 5. The reason for these inversions is that $R_{\mathrm{E},11} = -R_{\mathrm{H},11}$ for RGO_0 and $R_{\mathrm{E},2} = -R_{\mathrm{H},2}$ for RGO_1.

The reference solution $\mathrm{Re}[y_{j,\mathrm{reference}}(t)]$, $j = \mathrm{E}, \mathrm{H}$, which is expressed in integral form, is computed numerically using the fast Fourier transform (FFT) numerical code [31]. Therefore, it is difficult to extract and calculate the peaks of the backward transient scattering field components and their arrival times from $\mathrm{Re}[y_{j,\mathrm{reference}}(t)]$. In contrast, the peaks of the backward transient scattering field components and their arrival times can be calculated from (5) and (6), respectively. Also, the inversion phenomena for the peaks of the response waveforms can be analytically interpreted from (5) in conjunction with (A· 6), (A· 9), and (A· 14). From the above advantages over the reference solution, we can confirm the practicality of TD-SPT.

5.2 Effectiveness of Scatterer Information Estimation Method

In this section, we verify the effectiveness of the scatterer information estimation method proposed in Sect. 4.3 by substituting specific numerical values into the estimation formulae for four types of scatterer estimation $(\hat{\varepsilon}_{1r}, \hat{\varepsilon}_{2r}, \hat{h}, \hat{a})$ in the simulation model shown in Fig. 4 (a). The numerical parameters used in the simulation experiments are the numerical data for three sets of backward transient scattering field components listed in Table 1 and the distance $\overline{L}_{\mathrm{DGO}}$ (= QP) given in the caption of Fig. 5. The convergence degree and the upper limit of the number of iterations are set to $\varepsilon = 1.0 \times 10^{-9}$ and $I_{\mathrm{MAX}} = 100$, respectively.

First, we validate the effectiveness of the estimation method for E-polarization. Table 2 shows the set values, estimates, and estimation errors for the four types of scatterer information. The following equation was used to calculate the estimation errors.

$$\text{estimation error} = \left| \frac{\overline{X} - \hat{X}}{\overline{X}} \right| \quad \text{for } X = \varepsilon_{1r}, \varepsilon_{2r}, h, a. \tag{30}$$

Table 1 Numerical data for three sets of response waveforms of the backward transient scattering field components for both E- and H-polarizations calculated from (5) and (6). The numerical parameters used in the simulation experiments are the same as those used in Fig. 5. Here, the thickness h is 0.47091 m (= 0.23546a).

field components	peaks	arrival times
DGO	$\overline{\mathrm{Re}[y_{\mathrm{E,SPT,DGO}}(\bar{t}_{\mathrm{DGO}})]} = +0.2390252779110931$ $\overline{\mathrm{Re}[y_{\mathrm{H,SPT,DGO}}(\bar{t}_{\mathrm{DGO}})]} = +0.2390252779110931$	$\bar{t}_{\mathrm{DGO}} = 0.6337371666092792 \times 10^{-7}$ s
RGO_0	$\overline{\mathrm{Re}[y_{\mathrm{E,SPT,RGO}_0}(\bar{t}_{\mathrm{RGO}_0})]} = -0.5871699985606935 \times 10^{-1}$ $\overline{\mathrm{Re}[y_{\mathrm{H,SPT,RGO}_0}(\bar{t}_{\mathrm{RGO}_0})]} = +0.5871699985606935 \times 10^{-1}$	$\bar{t}_{\mathrm{RGO}_0} = 0.8005192142119303 \times 10^{-7}$ s
RGO_1	$\overline{\mathrm{Re}[y_{\mathrm{E,SPT,RGO}_1}(\bar{t}_{\mathrm{RGO}_1})]} = -0.8248377248296151 \times 10^{-1}$ $\overline{\mathrm{Re}[y_{\mathrm{H,SPT,RGO}_1}(\bar{t}_{\mathrm{RGO}_1})]} = +0.8248377248296151 \times 10^{-1}$	$\bar{t}_{\mathrm{RGO}_1} = 0.8947669938196241 \times 10^{-7}$ s

Table 2 Set values, estimates, and estimation errors of four types of scatterer information for E- and H-polarizations. The numerical parameters used in the simulation experiments are the same as those used in Fig. 5.

$\varepsilon = 1.0 \times 10^{-9}, I_{\mathrm{MAX}} = 100, I_{\mathrm{END}} = 6$

scatterer information	set values	estimates	estimation errors
$\varepsilon_{1\mathrm{r}}$	$\bar{\varepsilon}_{1r} = 1.0000000000000000$	$\hat{\varepsilon}_{1r} = 1.0000000000000000$	0.00000
$\varepsilon_{2\mathrm{r}}$	$\bar{\varepsilon}_{2r} = 9.0000000000000000$	$\hat{\varepsilon}_{2r} = 9.0000000000000568$	0.63159×10^{-14}
h	$\bar{h} = 0.4709128918171183$ m	$\hat{h} = 0.4709128918171170$ m	0.27112×10^{-14}
a	$\bar{a} = 2.0000000000000000$ m	$\hat{a} = 1.9999999999999858$ m	0.74385×10^{-14}

Since the number of iterations I_{END} is six, three types of estimates $(\hat{\varepsilon}_{2r}, \hat{h}, \hat{a})$ satisfy the convergence condition. From the high accuracy of four types of estimates $(\hat{\varepsilon}_{1r}, \hat{\varepsilon}_{2r}, \hat{h}, \hat{a})$ in Table 2, we can confirm the effectiveness of the estimation method for E-polarization in Sect. 4.3. In the simulation experiment, the estimates for the four types of scatterer information when the locations of a source point Q and an observation point P were swapped were identical to those in Table 2. The reason for the identical estimates is that the values of the numerical data listed in Table 1 and the distance $\overline{L}_{\mathrm{DGO}}$ do not change when the locations of the point Q and the point P are swapped.

Next, the effectiveness of the estimation method for H-polarization can be validated in the same way as for E-polarization, as described above. Since the estimation formulae for scatterer information derived in Sect. 4.2 are not affected by the sign of the AIRs, we obtained estimates and estimation errors identical to those in Table 2. Thus, we can numerically confirm the effectiveness of the estimation method for H-polarization in Sect. 4.3 and the polarization independence of the estimates.

5.3 Noise Tolerance of Estimation Method

In this section, we discuss the noise tolerance of the estimation method proposed in Sect. 4.3 when noise is added to the response waveforms of the backward transient scattering fields for E- and H-polarizations shown in Figs. 5 (a) and 5 (b).

The numerical parameters used in the calculations are shown in the caption of Fig. 5. The convergence degree and the upper limit of the number of iterations were set to $\varepsilon = 1.0 \times 10^{-9}$ and $I_{\mathrm{MAX}} = 100$, respectively. In the simulation experiments, noise was added to the signal data of the response waveform to generate new signal data mixed with the response waveform and noise. Specifically, the observation time range of $58\,\mathrm{ns} \le t \le 105\,\mathrm{ns}$ shown in Fig. 5 was divided by a step size of $\Delta t = 4.7 \times 10^{-13}\,\mathrm{s}$ to generate 10^5 pairs of noise-added signal data.

As a measure of the signal-to-noise power ratio, we used the following signal-to-noise ratio (SNR)

$$\mathrm{SNR} = 20 \log_{10} \frac{\mathrm{Signal}_{\mathrm{RMS}}}{\mathrm{Noise}_{\mathrm{RMS}}} \tag{31}$$

where $\mathrm{Signal}_{\mathrm{RMS}}$ is the strength of the response waveform signal and denotes the root mean square (RMS) of the amplitude values of the response waveform signal after removing the no-signal region. In this section, it is assumed that the noise is generated by the surface roughness at points Q_0 and R shown in Fig. 4 (a). The noise was modeled as an additive white Gaussian noise (AWGN) [32]. $\mathrm{Noise}_{\mathrm{RMS}}$ is the noise strength, which denotes the RMS of the AWGN amplitude values. To obtain an arbitrary SNR, the $\mathrm{Noise}_{\mathrm{RMS}}$ was superimposed on the $\mathrm{Signal}_{\mathrm{RMS}}$ to generate noise-added signal data.

First, we discuss the noise tolerance of the estimation method for E-polarization. Figure 6 shows the estimation errors and the number of iterations I_{END} for four types of estimates $(\hat{\varepsilon}_{1r}, \hat{\varepsilon}_{2r}, \hat{h}, \hat{a})$ as the SNR is varied from 10 to 50. The results for an SNR value of ∞ (no noise) are also included as a reference to compare the noise tolerance. The values of the estimation errors and I_{END} are the averages over 5×10^3 trials, at each SNR.

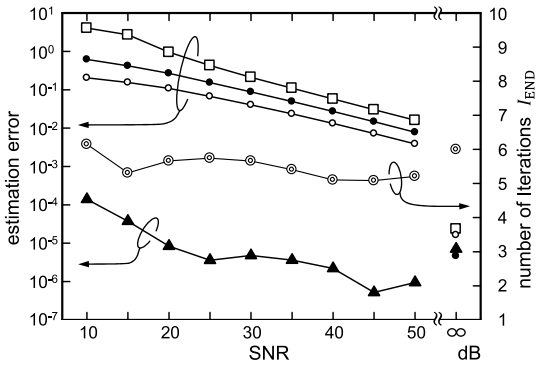

Fig. 6 Estimation errors for four types of estimates $(\hat{\varepsilon}_{1r}, \hat{\varepsilon}_{2r}, \hat{h}, \hat{a})$ for E- and H- polarizations when the SNR is varied under the condition that the convergence degree is set to $\varepsilon = 1 \times 10^{-9}$ and the number of significant digits of the numerical data for the arrival time is set to 8. The numerical parameters used in the simulation experiments are the same as those used in Fig. 5. ▲ ▲ ▲: $\hat{\varepsilon}_{1r}$, ● ● ●: $\hat{\varepsilon}_{2r}$, ○ ○ ○: $\hat{h}$, □ □ □: $\hat{a}$, ◎ ◎ ◎: I_{END}.

When the SNR value is ∞, the estimation errors for the estimates $(\hat{\varepsilon}_{1r}, \hat{\varepsilon}_{2r}, \hat{h}, \hat{a})$ are approximately 10^{-5}. Compared to the estimation errors for the estimates $(\hat{\varepsilon}_{1r}, \hat{\varepsilon}_{2r}, \hat{h}, \hat{a})$ shown in Table 2, the errors shown in Fig. 6 are significantly different. This difference is due to the fact that the significant digits of the arrival time used in the estimation in Table 2 are 16 digits, while the significant digits of the arrival time used in the estimation in Fig. 6 are 8 digits. Therefore, when the estimates $(\hat{\varepsilon}_{2r}, \hat{h}, \hat{a})$ are obtained from the noise-added response waveform signals, the estimation errors of these estimates deteriorate from about 10^{-5}. On the other hand, the estimate $\hat{\varepsilon}_{1r}$ is obtained by substituting $\overline{L}_{\mathrm{DGO}}$, $\overline{t}_{\mathrm{DGO}}$, and $\overline{t}_0$ into (11). The estimation accuracy of $\hat{\varepsilon}_{1r}$ depends on $\overline{t}_{\mathrm{DGO}}$ and not on the convergence degree ε or the I_{END}. Therefore, when the estimate $\hat{\varepsilon}_{1r}$ is obtained from the noise-added signal data, the estimation errors remain around 10^{-5}.

Figure 6 shows that the estimation errors of $\hat{\varepsilon}_{1r}$ are about 10^{-6} and 10^{-4} for SNR values of 50 and 10, respectively, and are nearly linear. The estimation errors of the estimates $(\hat{\varepsilon}_{2r}, \hat{h}, \hat{a})$ are about 10^{-2} and $2 \times 10^{-1} \sim 4 \times 10^{0}$ for SNR values of 50 and 10, respectively, and are linear. The I_{END} is independent of the SNR and is about 6. The estimation errors of the estimates $(\hat{\varepsilon}_{1r}, \hat{\varepsilon}_{2r}, \hat{h}, \hat{a})$ for H-polarization and the calculations for I_{END} are almost the same as those for E-polarization.

From the above discussions, the estimation method proposed in Sect. 4.3 has the following noise tolerance when the significant digits of the time increments and the convergence degree are set to 8 digits and $\varepsilon = 1.0 \times 10^{-9}$, respectively. The estimates $(\hat{\varepsilon}_{2r}, \hat{h}, \hat{a})$ for SNRs of ∞, 50, 30, and 10, the estimation errors are approximately 10^{-5}, 10^{-2}, 10^{-1}, and $2 \times 10^{-1} \sim 4 \times 10^{0}$, respectively. On the other hand, the

Table 3 Numerical data for three sets of response waveforms of the backward transient scattering field components for both E- and H-polarizations calculated from (5) and (6). The numerical parameters used in the simulation experiments are the same as those used in Fig. 5, except for the thickness h of a coating medium 2. Here, the thickness h is 0.79113 m (= $0.39557a$).

field components	peaks	arrival times
DGO	$\overline{\mathrm{Re}[y_{\mathrm{E,SPT,DGO}}(\bar{t}_{\mathrm{DGO}})]} = +0.2390252779110931$ $\overline{\mathrm{Re}[y_{\mathrm{H,SPT,DGO}}(\bar{t}_{\mathrm{DGO}})]} = +0.2390252779110931$	$\bar{t}_{\mathrm{DGO}} = 0.6337371666092792 \times 10^{-7}$ s
RGO_0	$\overline{\mathrm{Re}[y_{\mathrm{E,SPT,RGO}_0}(\bar{t}_{\mathrm{RGO}_0})]} = -0.5871699985606935\times 10^{-1}$ $\overline{\mathrm{Re}[y_{\mathrm{H,SPT,RGO}_0}(\bar{t}_{\mathrm{RGO}_0})]} = +0.5871699985606935\times 10^{-1}$	$\bar{t}_{\mathrm{RGO}_0} = 0.8005192142119303 \times 10^{-7}$ s
RGO_1	$\overline{\mathrm{Re}[y_{\mathrm{E,SPT,RGO}_1}(\bar{t}_{\mathrm{RGO}_1})]} = -0.7731026089010065\times 10^{-1}$ $\overline{\mathrm{Re}[y_{\mathrm{H,SPT,RGO}_1}(\bar{t}_{\mathrm{RGO}_1})]} = +0.7731026089010065\times 10^{-1}$	$\bar{t}_{\mathrm{RGO}_1} = 0.9588554839528558 \times 10^{-7}$ s

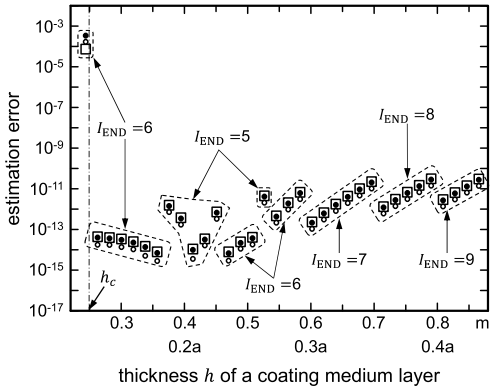

Fig. 7 Estimation errors for three types of estimates $(\hat{\varepsilon}_{2r}, \hat{h}, \hat{a})$ for E- and H-polarizations when the thickness h of a coating medium 2 is varied under the condition that the convergence degree ε is set to $\varepsilon = 1 \times 10^{-9}$. The numerical parameters used in the simulation experiments are the same as those used in Fig. 5, except for the thickness h. The minimum thickness h_c in (26) is 0.24983 m (= $0.12491a$). • • •: $\hat{\varepsilon}_{2r}$, ○ ○ ○: $\hat{h}$, □ □ □: $\hat{a}$.

estimation errors of the estimate $\hat{\varepsilon}_{1r}$ for SNRs of ∞, 50, 30, and 10 are approximately 10^{-5}, 10^{-6} 10^{-5}, and 10^{-4}, respectively.

5.4 Convergence Characteristics of Scatterer Information Estimation Method

In this section, we test the convergence characteristics of the scatterer information estimation method as the thickness h of a coating medium 2 is varied. The estimation accuracy of the estimate $\hat{\varepsilon}_{1r}$ does not depend on the convergence degree ε and the number of iterations I_{END}. In the following, we will discuss the convergence properties of the estimation method by calculating the estimation errors and the number of iterations I_{END} for the three types of scatterer information estimates $(\hat{\varepsilon}_{2r}, \hat{h}, \hat{a})$.

Figure 7 shows the estimation errors of the scatterer information for E-polarization and the number of iterations I_{END} for different thicknesses h under the condition that the convergence degree is set to $\varepsilon = 1 \times 10^{-9}$. The numerical parameters used in the simulation experiments are the numerical data of three sets of backward transient scattering field components obtained analytically from TD-SPT and the distance $\overline{L}_{\mathrm{DGO}}$ (= QP) given in the caption of Fig. 5. The thickness h was set to range from 0.24487 m (= $0.12244a$) to 0.86648 m (= $0.43324a$), including the minimum thickness h_c (= 0.24983 m (= $0.12491a$)) in (26).

From Fig. 7, when the thickness h satisfies the applicable condition in (27) ($h \geq h_c$), the estimation errors are distributed in the range of 10^{-14} to 10^{-10}, and the I_{END} varies from 5 to 9. The thickness with minimum errors was h = 0.47091 m (= $0.23546a$), and the thickness with maximum errors was h = 0.79113 m (= $0.39557a$). When the thickness h did not satisfy the applicable condition in (27) ($h < h_c$), the estimation errors were distributed in the range of 10^{-4} to 10^{-3}, and the I_{END} was 6. The estimation errors of the scatterer information for the H-polarization and the I_{END} were exactly the same as those for the E-polarization.

From the above discussions, it is estimated that for E- and H-polarizations, under the application conditions of Sect. 4.4, when the convergence degree is set to $\varepsilon = 1 \times 10^{-9}$ and the estimation method of Sect. 4.3 is used, the estimates $(\hat{\varepsilon}_{2r}, \hat{h}, \hat{a})$ converge to an accuracy between 10^{-14} and 10^{-10} with a number of iterations of one digit.

5.5 Method for Controlling the Estimation Accuracy

The accuracy of the estimate $\hat{\varepsilon}_{1r}$ is independent of the convergence degree ε and the number of iterations I_{END}. In this section, we will discuss how to control the estimation accuracy of three types of scatterer information estimates $(\hat{\varepsilon}_{2r}, \hat{h}, \hat{a})$. For the simulation experiments, we selected two values of h = 0.47091 m (= $0.23546a$) and h = 0.79113 m (= $0.39557a$) for the thickness of a coating medium 2, which gave the minimum and maximum estimation errors in Fig. 7. Tables 1 and 3 show the numerical data of three sets of backward transient scattering field components for both E- and H-polarizations for thicknesses h = 0.47091 m and h = 0.79113 m, respectively.

Figure 8 shows the estimation errors of the estimates $(\hat{\varepsilon}_{2r}, \hat{h}, \hat{a})$ and the I_{END} for E-polarization for different degrees of convergence ε under the condition that the thicknesses are set to h = 0.47091 m and h = 0.79113 m, respectively, as well as auxiliary lines representing their evolution.

First, the case h = 0.47091 m is discussed. We observe that when the value of ε is decreased (increased), the errors become smaller (larger). If the I_{END} is the same, there is no change in the error when the value of ε is changed. Referring to the dashed auxiliary line (– – – – –), the errors tend to decrease by one order of magnitude when the ε is decreased by one order of magnitude. The calculations of the estimation errors for the estimates $(\hat{\varepsilon}_{2r}, \hat{h}, \hat{a})$ for H-polarization were exactly the same as for E-polarization. From the above

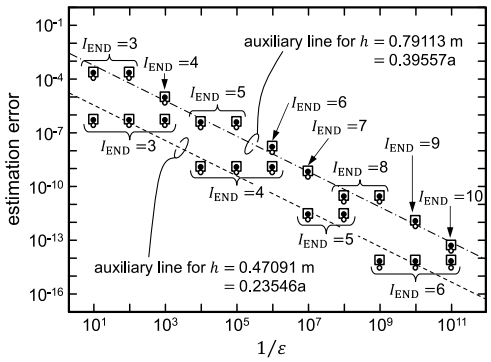

Fig. 8 Estimation errors for three types of estimates $(\hat{\varepsilon}_{2r}, \hat{h}, \hat{a})$ for E- and H-polarizations when the convergence degree ε is varied under the condition of the fixed thickness h of a coating medium 2. The numerical parameters used in the simulation experiments are the same as those used in Fig. 5, except for the thickness h. Here, the thicknesses are set to h = 0.47091 m (= $0.23546a$) and h = 0.79113 m (= $0.39557a$), respectively. • • •: $\hat{\varepsilon}_{2r}$, ○ ○ ○: $\hat{h}$, □ □ □: $\hat{a}$.

discussions, we can confirm that the estimation accuracy of the estimates $(\hat{\varepsilon}_{2r}, \hat{h}, \hat{a})$ for both E- and H-polarizations can be controlled by varying the value of the ε.

Next, the case h = 0.79113 m is discussed. The trend of the changes in the estimation errors of the estimates $(\hat{\varepsilon}_{2r}, \hat{h}, \hat{a})$ for $1/\varepsilon$ is shown by the single dash-dotted auxiliary line (–·–·–). Compared to the broken auxiliary line (– – – – –), the single dash-dotted auxiliary line (–·–·–) has an almost identical slope, with the errors increasing by about 10^2. The trend of the error variations in the estimates $(\hat{\varepsilon}_{2r}, \hat{h}, \hat{a})$ for H-polarization was the same as for E-polarization. The same slope of the two auxiliary lines indicates that the estimation accuracy of the estimates $(\hat{\varepsilon}_{2r}, \hat{h}, \hat{a})$ for both E- and H-polarizations for h = 0.79113 m can be controlled by changing the value of the ε.

From the above discussions, we can confirm the effectiveness of the control method for the estimation accuracy.

6. Conclusions

In this paper, we have proposed the scatterer information estimation method using numerical data for the response waveform of a backward transient scattering field for both E- and H-polarizations when a 2-D coated metal cylinder is selected as a scatterer. It was assumed that a line source and an observation point were placed at different locations.

Specifically, the four types of scatterer information estimation formulae, namely the relative permittivity of a surrounding medium, the relative permittivity of a coating medium layer and its thickness, and the radius of a coated metal cylinder, have been derived from the AIRs using the TD-SPT. We obtained the estimates by substituting the numerical data for three sets of the peaks of the response waveforms of the backward transient scattering field components and their arrival times and the numerical data of the distance between the source point and the observation point into the estimation formulae, followed by the iterative calculations.

Furthermore, we derived the minimum thickness of a coating medium layer for which the estimation method is valid, and proposed two kinds of applicable conditions for the estimation method. By comparing the estimates with the set values, we verified the effectiveness of the scatterer information estimation method proposed in this paper. We also discussed the noise tolerance and convergence characteristics of the estimation method and the method of controlling the estimation accuracy.

In the future, a new method for estimating scatterer information when a line source and an observation point are placed at the same location will be investigated.

References

[1] J.B. Keller, "Diffraction by a convex cylinder," I.R.E. Trans. Antennas Propagat., vol.AP-4, no.3, pp.312–321, July 1956. DOI: 10.1109/tap.1956.1144427
[2] P.H. Pathak, "An asymptotic analysis of the scattering of plane waves by a smooth convex cylinder," Radio Science, vol.14, no.3, pp.419–435, May-June 1979.
[3] P.H. Pathak, W.D. Burnside, and R.J. Marhefka, "A uniform GTD analysis of the diffraction of electromagnetic waves by a smooth convex surface," IEEE Trans. Antennas Propagat., vol.AP-28, no.5, pp.631–642, Sept. 1980. DOI: 10.1109/tap.1980.1142396
[4] R.C. Hansen, ed., Geometric Theory of Diffraction, IEEE Press, New York, 1981.
[5] N. Wang, "Electromagnetic scattering from a dielectric-coated circular cylinder," IEEE Trans. Antennas Propagat., vol.AP-33, no.9, pp.960–963, Sept. 1985. DOI: 10.1109/TAP.1985.1143696
[6] G.L. James, ed., Geometrical Theory of Diffraction for Electromagnetic Waves, 3rd ed., Peter Peregrinus, London, 1986. DOI: 10.1049/pbew001e
[7] H.-T. Kim and N. Wang, "UTD solution for electromagnetic scattering by a circular cylinder with thin lossy coatings," IEEE Trans. Antennas Propagat., vol.37, no.11, pp.1463–1472, Nov. 1989. DOI: 10.1109/8.43566
[8] P. Hussar and R. Albus, "On the asymptotic frequency behavior of uniform GTD in the shadow region of a smooth convex surface," IEEE Trans. Antennas Propagat., vol.39, no.12, pp.1672–1680, Dec. 1991.
[9] L.B. Felsen and N. Marcuvitz, eds., Radiation and Scattering of Waves, IEEE Press, New York, 1994. DOI: 10.1109/9780470546307
[10] T.B.A. Senior and J.L. Volakis, eds., Approximate Boundary Conditions in Electromagnetics, IEE, London, 1995. DOI: 10.1049/pbew041e
[11] P.E. Hussar, "A uniform GTD treatment of surface diffraction by impedance and coated cylinders," IEEE Trans. Antennas Propagat., vol.46, no.7, pp.998–1008, July 1998. DOI: 10.1109/8.704801
[12] H. Vollmer and E.J. Rothwell, "Resonance series representation of the early-time field scattered by a coated cylinder," IEEE Trans. Antennas Propagat., vol.52, no.8, pp.2186–2190, Aug. 2004. DOI: 10.1109/TAP.2004.832331
[13] T. Ida and T. Ishihara, "Novel high-frequency asymptotic solutions in the transition regions near geometrical boundaries and near caustics for scattering by a dielectric cylinder," IEICE Trans. Electron., vol.E87-C, no.9, pp.1550–1559, Sept. 2004.
[14] T. Ida and T. Ishihara, "Novel high-frequency uniform asymptotic solution for scattered field by a conducting cylinder," IEICE Trans. Electron. (Japanese Edition), vol.J87-C, no.10, pp.754–767, Oct. 2004.
[15] T. Ida, T. Ishihara, and K. Goto, "Frequency-domain and time-domain novel uniform asymptotic solutions for scattered fields by an impedance cylinder and a dielectric cylinder," IEICE Trans. Electron., vol.E88-C, no.11, pp.2124–2135, Nov. 2005. DOI: 10.1093/ietele/e88-c.11.2124

[16] J. Sun and L.-W. Li, "Dispersion of waves over a PEC cylinder coated with two-layer lossy dielectric materials," IEEE Trans. Antennas Propagat., vol.55, no.3, pp.877–881, March 2007. DOI: 10.1109/TAP.2007.891856
[17] G. Roqueta, L. Jofre, and M.Q. Feng, "Analysis of the electromagnetic signature of reinforced concrete structures for nondestructive evaluation of corrosion damage," IEEE Trans. Instrum. Meas., vol.61, no.4, pp.1090–1098, April 2012. DOI: 10.1109/TIM.2011.2174106
[18] M. Nishimoto and Y. Naka, "Analysis of transient scattering by a metal cylinder covered with inhomogeneous lossy material for nondestructive testing," IEICE Trans. Electron., vol.E101-C, no.1, pp.44–47, Jan. 2018. DOI: 10.1587/transele.E101.C.44
[19] M. Nishimoto, B.P.A. Rohman, Y. Naka, and K. Ogata, "Corrosion state estimation of rebar in reinforced concrete using ultra-wideband radar," IEICE Trans. Electron. (Japanese Edition), vol.J104-C, no.11, pp.319–325, Nov. 2021. DOI: 10.14923/transelej.2021JCI0001
[20] K. Hagiwara, K. Goto, S. Tokumaru, L. Okada, and Y. Takeno, "Novel time-domain asymptotic-numerical solutions for transient scattered electric field from a coated cylinder covered with a thick dielectric medium," IEICE Electron. Express, vol.14, no.5, 20170085, pp.1–10, March 2017. DOI: 10.1587/elex.14.20170085
[21] T. Kawano and K. Goto, "Novel time-domain asymptotic-numerical solution for forward transient scattered magnetic field from a coated metal cylinder," IEICE Electron. Express, vol.17, no.18, 20200246, pp.1–5, Sept. 2020. DOI: 10.1587/elex.17.20200246
[22] T. Kawano and K. Goto, "Novel time-domain asymptotic-numerical solution for backward transient scattered magnetic field from a coated metal cylinder," IEICE Electron. Express, vol.18, no.2, 20200399, pp.1–6, Jan. 2021. DOI: 10.1587/elex.18.20200399
[23] T. Kawano and K. Goto, "Interpretation method of inversion phenomena on backward transient scattered field components by a coated metal cylinder," IEICE Trans. Electron., vol.E105-C, no.9, pp.389–397, Sept. 2022. DOI: 10.1587/transele.2021ECP5051
[24] K. Goto and T. Kawano, "A study on the polarization dependence of backward transient scattering by a two-dimensional coated conducting cylinder using the TD-SPT," Proc. ICEAA 2022, p.26, Cape Town, Sept. 2022. DOI: 10.1109/ICEAA49419.2022.9900030
[25] T. Kawano and K. Goto, "A novel time-domain asymptotic solution for a backward transient scattered electric field by a coated metal cylinder," Proc. ICEAA 2022, pp.27–30, Cape Town, Sept. 2022. DOI: 10.1109/ICEAA49419.2022.9899979
[26] K. Goto and T. Kawano, "An interpretation method on amplitude intensities for response waveforms of backward transient scattered field components by a 2-D coated metal cylinder," IEICE Trans. Electron., vol.E106-C, no.4, pp.118–126, April 2023. DOI: 10.1587/transele.2022REP0001
[27] K. Goto, T. Kawano, M. Kato, and H. Koriyama, "Estimation method of scatterer information using the response waveform of a backward transient scattered magnetic field by the TD-SPT—Case where source and observation points are located at different locations—," The Papers of Technical Meeting on Electromagnetic Theory, IEE Japan, EMT-22-34, pp.19–27, June 2022.
[28] M. Abramowitz and I.A. Stegun, eds., Handbook of Mathematical Functions, 10th ed., Dover, New York, 1972.
[29] Federal Communications Commission (FCC), ed., First report and order: Revision of part 15 of the commission's rules regarding ultra-wideband transmission systems, FCC 02-48, Washington, D.C., April 2002.
[30] C.A. Balanis, ed., Advanced Engineering Electromagnetics, John Wiley & Sons, New Jersey, 1989.
[31] E.O. Brigham, ed., The Fast Fourier Transform, Prentice-Hall, New Jersey, 1974.
[32] Y. Kamiyama, ed., Digital Wireless Communication Technologies with MATLAB, Corona Publishing, Tokyo, 2020 (in Japanese).
[33] R.G. Kouyoumjian and P.H. Pathak, "A uniform geometrical theory of diffraction for an edge in a perfectly conducting surface," Proc. IEEE, vol.62, no.11, pp.1448–1461, Nov. 1974.

Appendix: Time-Domain Saddle-Point Technique (TD-SPT)

A TD-SPT on the z-component of a backward transient scattering field for both E- and H-polarizations $y_j(\rho_0,\ \phi_0,\ \rho \neq \rho_0,\ \phi = \phi_0;\ t) = y_j(t)$, $j = \mathrm{E}, \mathrm{H}$ from a coated metal cylinder is given by [23]

$$\begin{aligned} y_j(t) &\sim y_{j,\text{TD-SPT}}(t) \\ &= y_{j,\text{SPT,DGO}}(t) + \sum_{p=0}^{M_j} y_{j,\text{SPT,RGO}_p}(t), \quad j = \mathrm{E}, \mathrm{H}. \end{aligned} \tag{A·1}$$

In (A·1), $y_{j,\text{SPT,DGO}}(t)$ and $y_{j,\text{SPT,RGO}_p}(t)$ are the DGO and RGO solutions, respectively, and are given by [23]

$$\begin{aligned} y_{j,\text{SPT},\ell}(t) &= D(\omega_{s,\ell}) A_{j,\ell}\, \mathrm{Re}[\mathrm{erf}\, \beta(\omega_{s,\ell})] s\left(t - \frac{L_\ell}{c_1}\right), \\ \ell &= \mathrm{DGO}, \mathrm{RGO}_p, \quad \text{for } \frac{L_\ell}{c_1} \le t \le 2t_0 + \frac{L_\ell}{c_1} \end{aligned} \tag{A·2}$$

where $D(\omega)$ and c_1 denote a common factor and the speed of light in a surrounding medium 1, respectively, and $\omega_{s,\ell}$ is a saddle point [23]. The notations erf z and $s(t)$ denote the error function in (4) [28] and the pulse source in (1), respectively. The symbol $\beta(\omega)$ is defined in (3) and M_j is the number of truncated terms in the RGO series.

$$D(\omega) = \sqrt{\frac{c_1}{8\pi\omega}} \exp(i\pi/4) \tag{A·3}$$

$$c_1 = \frac{1}{\sqrt{\varepsilon_1 \mu_0}} = \frac{c_0}{\sqrt{\varepsilon_{1r}}}, \quad c_0 = \frac{1}{\sqrt{\varepsilon_0 \mu_0}} \tag{A·4}$$

$$\omega_{s,\ell} = \omega_0 - i\frac{1}{2d^2}\left(t - t_0 - \frac{L_\ell}{c_1}\right), \ \ell = \mathrm{DGO}, \mathrm{RGO}_p. \tag{A·5}$$

The notations $D(\omega_{s,\ell}) A_{j,\ell}\, \mathrm{Re}[\mathrm{erf}\, \beta(\omega_{s,\ell})]$ and L_ℓ denote the amplitude and distance functions of $y_{j,\text{SPT},\ell}(t)$ in (A·2), respectively.

A.1 Symbols $A_{j,\text{DGO}}$ and L_{DGO} of DGO in (A·2)

The symbols $A_{j,\text{DGO}}$ and L_{DGO} of DGO propagating along the path Q→P from a source point Q to an observation point P (see Fig. 2) are given by [23]

$$A_{j,\text{DGO}} = \hat{A}_{j,\text{DGO}} \tag{A·6}$$

$$\hat{A}_{j,\text{DGO}} = \sqrt{\frac{1}{L_{\text{DGO}}}} \tag{A·7}$$

$$L_{\text{DGO}} = |\rho_0 - \rho| = \mathrm{QP} \tag{A·8}$$

where $\hat{A}_{j,\text{DGO}}$ is a divergence factor of DGO [33].

A.2 Symbols A_{j,RGO_0} and L_{RGO_0} of RGO_0 in (A· 2)

The symbols A_{j,RGO_0} and L_{RGO_0} of RGO_0 propagating along the path Q→Q_0→P, which is emitted at the point Q and reflected at the point Q_0 on a coating surface defined by radius $\rho = a$ before arriving at the point P (see Fig. 2), are given by [23]

$$A_{j,\mathrm{RGO}_0} = \hat{A}_{j,\mathrm{RGO}_0} R_{j,11} \tag{A· 9}$$

$$\hat{A}_{j,\mathrm{RGO}_0} = \sqrt{\frac{a}{aL_< + aL_> + 2L_< L_>}} \tag{A· 10}$$

$$L_{\mathrm{RGO}_0} = L_1 + L_2 = L_< + L_> \tag{A· 11}$$

$$L_1 = \rho_0 - a = \mathrm{QQ}_0, \quad L_2 = \rho - a = \mathrm{Q}_0\mathrm{P}. \tag{A· 12}$$

The notation $\hat{A}_{j,\mathrm{RGO}_0}$ denotes a divergence factor of RGO_0 [2], [3], and $L_<$ ($L_>$) is a symbol for the smaller (larger) in L_1 and L_2. In (A· 9), $R_{j,11}$ is a reflection coefficient on the *convex side* at the point Q_0 on the coating surface (see Fig. 2) and is defined by

$$R_{j,11} = \begin{cases} -\dfrac{\sqrt{\varepsilon_{2r}} - \sqrt{\varepsilon_{1r}}}{\sqrt{\varepsilon_{2r}} + \sqrt{\varepsilon_{1r}}} & \text{for } j = \mathrm{E} \\ +\dfrac{\sqrt{\varepsilon_{2r}} - \sqrt{\varepsilon_{1r}}}{\sqrt{\varepsilon_{2r}} + \sqrt{\varepsilon_{1r}}} & \text{for } j = \mathrm{H} \end{cases}. \tag{A· 13}$$

A.3 Symbols A_{j,RGO_p} and L_{RGO_p} of RGO_p, $p = 1, 2, \cdots, M_j$ in (A· 2)

The symbols A_{j,RGO_p} and L_{RGO_p} of RGO_p, $p = 1, 2, \cdots, M_j$ propagating along the path Q→p(Q_0→R→)Q_0 →P, which is emitted at the point Q and then reflected p times at the point R including the multiple reflection effect p(Q_0→R→)Q_0 before arriving at the point P (see Fig. 2), are given by [23]

$$A_{j,\mathrm{RGO}_p} = \hat{A}_{j,\mathrm{RGO}_p} T_{j,12} (R_{j,2})^p (R_{j,22})^{p-1} T_{j,21} \tag{A· 14}$$

$$\hat{A}_{j,\mathrm{RGO}_p} = \sqrt{\frac{a}{aL_< + aL_> + 2L_< L_> + D_p}} \tag{A· 15}$$

$$D_p = \frac{p(a + L_<)(a + L_>)(2h)}{a - h} \sqrt{\frac{\varepsilon_{1r}}{\varepsilon_{2r}}} \tag{A· 16}$$

$$L_{\mathrm{RGO}_p} = L_< + p\sqrt{\frac{\varepsilon_{2r}}{\varepsilon_{1r}}}(2h) + L_>. \tag{A· 17}$$

The notation $\hat{A}_{j,\mathrm{RGO}_p}$ is a divergence factor of RGO_p. In (A· 14), $T_{j,12}$ ($T_{j,21}$) denotes a transmission coefficient from medium 1 (medium 2) to medium 2 (medium 1) at the point Q_0 (see Fig. 2) and is given by

$$T_{j,12} = \begin{cases} \dfrac{2\sqrt{\varepsilon_{1r}}}{\sqrt{\varepsilon_{2r}} + \sqrt{\varepsilon_{1r}}} & \text{for } j = \mathrm{E} \\ \dfrac{2\sqrt{\varepsilon_{2r}}}{\sqrt{\varepsilon_{2r}} + \sqrt{\varepsilon_{1r}}} & \text{for } j = \mathrm{H} \end{cases} \tag{A· 18}$$

$$T_{j,21} = \begin{cases} \dfrac{2\sqrt{\varepsilon_{2r}}}{\sqrt{\varepsilon_{2r}} + \sqrt{\varepsilon_{1r}}} & \text{for } j = \mathrm{E} \\ \dfrac{2\sqrt{\varepsilon_{1r}}}{\sqrt{\varepsilon_{2r}} + \sqrt{\varepsilon_{1r}}} & \text{for } j = \mathrm{H} \end{cases}. \tag{A· 19}$$

The notations $R_{j,2}$ and $R_{j,22}$ denote a reflection coefficient at the point R and that on the *concave side* at the point Q_0 on the coating surface (see Fig. 2) and are defined by

$$R_{j,2} = \begin{cases} -1 & \text{for } j = \mathrm{E} \\ +1 & \text{for } j = \mathrm{H} \end{cases} \tag{A· 20}$$

$$R_{j,22} = \begin{cases} +\dfrac{\sqrt{\varepsilon_{2r}} - \sqrt{\varepsilon_{1r}}}{\sqrt{\varepsilon_{2r}} + \sqrt{\varepsilon_{1r}}} & \text{for } j = \mathrm{E} \\ -\dfrac{\sqrt{\varepsilon_{2r}} - \sqrt{\varepsilon_{1r}}}{\sqrt{\varepsilon_{2r}} + \sqrt{\varepsilon_{1r}}} & \text{for } j = \mathrm{H} \end{cases}. \tag{A· 21}$$

The HF asymptotic solution for a backward transient scattering field component in (A· 2), which constitutes the TD-SPT in (A· 1), satisfies the reciprocity principle [30], since the same solution is obtained when the locations of a source point Q and an observation point P are swapped.

Keiji Goto received the B.E. and M.E. degrees (equivalents) from the National Defense Academy of Japan, Yokosuka, Japan, in 1984 and 1989, respectively, and the D.E. degree from the University of Tsukuba, Tsukuba, Japan, in 2001. From 1991 to 1996, he was a Researcher at the National Defense Academy of Japan. From 1996 to 2004, he was worked as a Researcher at the Japan Ground Self-Defense Force and at the Defense Agency (now the Ministry of Defense) in Japan. Since March 2004, he has been with the National Defense Academy of Japan, where he is currently a Professor. His current research interests include high-frequency scattering in the frequency and time domains. Dr. Goto received the Paper Presentation Award from the Institute of Electrical Engineers of Japan in 1993.

Toru Kawano received the B.E., M.E., and D.E. degrees in electrical engineering from Hosei University, Tokyo, Japan, in 1995, 1997, and 2001, respectively. Since April 2001, he has been with the National Defense Academy of Japan, where he is currently an Associate Professor. His current research interests include the scattering and propagation of electromagnetic waves, and antennas. Dr. Kawano received the Paper Presentation Award from the Institute of Electrical Engineers of Japan in 2008.

Munetoshi Iwakiri received the B.E. degree in Computer Science in 1993 and the M.E. degree in Mathematics and Computer Science in 1998 from the National Defense Academy of Japan, Yokosuka, Japan. In 1999, he joined the Department of Computer Science, the National Defense Academy of Japan, as a Research Associate. In 2002, he received the D.E. degree from Keio University, Tokyo, Japan. In 2005, he became a Lecturer and in 2015, he became an Associate Professor in the same institution. His research interests include multimedia processing and information security.

Tsubasa Kawakami is currently a member of the undergraduate course of the Department of Communications Engineering at the National Defense Academy of Japan, Yokosuka, Japan. Her current research interests include high-frequency scattering of electromagnetic waves.

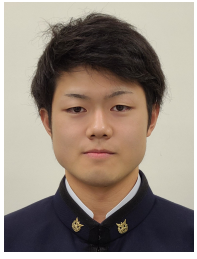

Kazuki Nakazawa is currently a member of the undergraduate course of the Department of Communications Engineering at the National Defense Academy of Japan, Yokosuka, Japan. His current research interests include high-frequency scattering of electromagnetic waves.